

# MUSCLE-UPS: Improved Approximations of the Matter Field with the Extended Press-Schechter Formalism and Lagrangian Perturbation Theory

Federico Tosone,<sup>1,2\*</sup> Mark C. Neyrinck,<sup>3,4,5</sup> Benjamin R. Granett,<sup>6,7,8</sup>  
Luigi Guzzo,<sup>6,7,8</sup> Nicola Vittorio<sup>1,2</sup>

<sup>1</sup>*Dipartimento di Fisica, Università di Roma Tor Vergata, Via della Ricerca Scientifica 1, I-00133, Roma, Italy*

<sup>2</sup>*INFN Sezione di Roma Tor Vergata, Via della Ricerca Scientifica 1, I-00133, Roma, Italy*

<sup>3</sup>*Ikerbasque, the Basque Foundation for Science*

<sup>4</sup>*Dept. of Physics, University of the Basque Country UPV/EHU, Bilbao, Spain*

<sup>5</sup>*Donostia International Physics Center, San Sebastián, Spain*

<sup>6</sup>*Università degli Studi di Milano, via G. Celoria 16, 20133 Milano, Italy*

<sup>7</sup>*INAF - Osservatorio Astronomico di Brera, via Brera 28, 20122 Milano, Italy*

<sup>8</sup>*INFN Sezione di Milano, Via G. Celoria 16, 20133, Milano, Italy*

Accepted XXX. Received YYY; in original form ZZZ

## ABSTRACT

Lagrangian algorithms to simulate the evolution of cold dark matter (CDM) are invaluable tools to generate large suites of mock halo catalogues. However, their precision may not be up to the challenge of upcoming surveys. In this paper, we first show that the main limitation of current schemes is their inability to model the evolution of overdensities in the initial density field, a limit that can be circumvented by detecting halo particles in the initial conditions. We thus propose a new scheme, dubbed MUSCLE-UPS, which reproduces the results from Lagrangian perturbation theory on large scales, while improving the modelling of the overdensities on small scales. MUSCLE-UPS uses the extended Press and Schechter (EPS) formalism, adapted to a Lagrangian picture. For regions exceeding a collapse threshold in the density smoothed at a radius  $R$ , we consider all particles within a radius  $R$  collapsed. Exploiting a multi-scale smoothing of the initial density, we build a halo catalogue on the fly by optimizing the selection of halo candidates. This allows us to generate a density field with a halo mass function that matches one measured in  $N$ -body simulations. We further explicitly gather particles in each halo together in a profile, providing a numerical, Lagrangian-based implementation of the halo model. Compared to previous semi-analytical Lagrangian methods, we find that MUSCLE-UPS improves the recovery of the statistics of the density field at the level of the probability density function (PDF), the power spectrum, and the cross correlation with the  $N$ -body result.

**Key words:** keyword1 – keyword2 – keyword3

## 1 INTRODUCTION

Structures in the Universe formed through gravitational clustering around perturbations in an almost homogeneous initial matter distribution. These seeds eventually became haloes, the most gravitationally bound structures in the Universe, and they set the stage for the formation of the cosmic web wrapped around them.

An insight into this process was offered by the Lagrangian picture: if CDM is treated as an ideal, pressure-

less and self-gravitating fluid, the formation of caustics is expected (Buchert 1992). This was also confirmed by numerical simulations based on the same formalism (Bouchet et al. 1995): perturbative schemes such as the Zel’dovich approximation (ZA) and second-order Lagrangian perturbation theory (2LPT) are so effective in reproducing the cosmic web (Bond et al. 1996), that they became customary techniques for the generation of mock galaxy catalogues. They are adopted by many codes such as PEAK-PATCH (Bond & Myers 1996; Stein et al. 2019), PINOCCHIO (Monaco et al. 2002, 2013), P<sub>THALOES</sub> (Scoccimarro & Sheth 2002), COLA (Tassev et al. 2013), HALOGEN (Avila et al. 2015), PATCHY

\* E-mail: federico.tosone@roma2.infn.it

(Kitaura et al. 2014), EZMOCKS (Chuang et al. 2015). The reason behind the success of semi-analytical schemes is that they allowed to build hundreds of simulated realizations for a given cosmology, which is still prohibitive for  $N$ -body codes. Moreover, these approximate schemes have opened up the path to the reconstruction of initial conditions by forward Bayesian methodologies (Jasche & Wandelt 2013; Kitaura 2013; Leclercq et al. 2015; Bos et al. 2019) or reconstructions based on reversing gravity evolution (Padmanabhan et al. 2012).

Despite their importance and widespread use, the progress in Lagrangian semi-analytical techniques has been slow, due to the intrinsic limitations of perturbation theory. First, it is accurate only for small perturbations, thus failing at low redshift and small scales. Secondly, it moves particles only according to the initial potential, so it becomes inaccurate when caustics occur and particle trajectories overlap. An advance came when Neyrinck (2013) proposed a non-perturbative technique based on the spherical collapse model (SC), which provides a better description of voids and overdensities in the simulations. The SC approach can be combined with 2LPT, valid on large scales; the resulting technique was dubbed Augmented Lagrangian Perturbation Theory (ALPT). It performs remarkably well at the level of fundamental statistics of the CDM density field (Kitaura & Hess 2013), and has been extensively used for the generation of mock catalogues, e.g. providing the basis for the the widely used PATCHY mocks for the Baryon Oscillation Spectroscopic Survey Kitaura et al. (2016). Later, Neyrinck (2016) proposed a new scheme named MUSCLE, an improved non-perturbative method to detect halo particles through a multi-scale smoothing process based on the SC criterion. This approach has the benefit of arguable conceptual clarity, and recovers the linear power spectrum much better than SC on large scales, while being comparable to ALPT with respect to the small scale clustering.

The possibility to improve Lagrangian non-perturbative techniques motivated our recent study (Tosone et al. 2020), where we measured the statistics of the density field generated from a displacement field that encodes the same PDF and power spectrum of the exact displacement measured from the  $N$ -body. We found only marginal benefits, with results not better than MUSCLE. We concluded that any improvement should come from a multi-scale approach. This is in fact the subject of the work presented here, which we regard as a significant step forward, compared to existing schemes in the literature.

After briefly recalling the basic approximation schemes in Section 2 and outlining the methodology in Section 3, in Section 4 we show the reasoning that led to our proposed approach. We start by considering truncated schemes of Lagrangian approximations, as we confirm that they perform comparably well, if not better, than non-truncated schemes (Coles et al. 1993). This suggests that the main limitation of semi-analytical techniques is their lack of predictivity for overdense regions. We further state our point about the importance of overdensities in Section 5, where we show that a better identification of halo particles in the initial conditions is enough to improve substantially the approximation of the displacement field.

To this end in Section 6 we propose a predictive scheme which is based on the EPS formalism (Zentner 2007)

adapted to the Lagrangian picture. A voxel (i.e. a cubic cell on the mesh grid) that exceeds a collapse threshold in the density smoothed at some scale  $R$  should collapse along with other voxels within (some multiple of)  $R$ . We dub this technique MULTISCALE SPHERICAL COLLAPSE LAGRANGIAN EVOLUTION USING PRESS-SCHECHESTER (MUSCLE-UPS). To correctly recover the power spectrum expected from linear theory on large scales, we interpolate the displacement field generated through MUSCLE-UPS on small scales with truncated 2LPT (T2LPT) on large scales, using the same technique of ALPT. The main results of this new scheme is the ability to improve the recovery of the power spectrum at quasi-linear scales, the recovery of the high-density tail of the PDF and better the cross-correlation with the density field in the quasi-linear regime.

Since MUSCLE-UPS is based on a multi-scale smoothing of the initial conditions, in §7 we propose a method to build a halo catalogue based on the smoothing scale of collapse of each voxel and the density of each proto-halo patch. By exploiting the freedom in the choice of merging events, we can optimize the construction of a halo catalogue by matching it to a target HMF as measured in  $N$ -body simulations. Finally, we show how to use this halo catalogue to implement the halo model (Peacock & Smith 2000; Seljak 2000), which further improves the results for the power spectrum. We show the results in Section 8, and conclude in Section 9.

## 2 THEORY

### 2.1 Zel'dovich Approximation

The Lagrangian description of structure formation consists of finding the field  $\Psi$  that maps an initial grid of particles, with uniform density  $\rho_0$ , from their coordinates  $\mathbf{q}$  to the final Eulerian positions

$$\mathbf{x}(\mathbf{q}) = \mathbf{q} + \Psi(\mathbf{q}). \quad (1)$$

The transformation from Eulerian density to Lagrangian density must satisfy the condition

$$\rho(\mathbf{x})d^3x = \rho_0d^3q, \quad (2)$$

which can be recast in terms of the Jacobian of the transformation

$$\left\| \frac{d^3x}{d^3q} \right\| = J = \frac{1}{1 + \delta}, \quad (3)$$

that is equivalent to

$$1 + \delta = \frac{1}{\left\| \delta_{ij}^{(k)} + \Psi_{i,j} \right\|}, \quad (4)$$

where  $\Psi_{i,j}$  stands for the  $j$ -th derivative of the  $i$ -th component of the displacement vector, and  $\delta_{ij}^{(k)}$  is a Kronecker delta.

From Eq. (4) one can immediately see that a perturbative treatment involves only the scalar component of  $\psi$  at first order, defined as  $\psi = \nabla \cdot \Psi$ , and it reads

$$\psi^{(1)} = -\delta^{(1)}(\mathbf{q}, \tau), \quad (5)$$

commonly known as the Zel'dovich Approximation (ZA). If we assume that the displacement field is irrotational, it can be expressed as a function of a displacement potential

$$\Psi = -\nabla\phi. \quad (6)$$

In the ZA we can define a displacement potential  $\phi^{(1)}$  that allows us to define a matrix  $\Psi_{i,j}^{(1)} = -\phi_{,ij}^{(1)}$ , which upon diagonalization yields for Eq. (4) (see Appendix A)

$$1 + \delta^{(1)}(\mathbf{q}, \tau) = \frac{1}{\|(1 - \lambda_1)(1 - \lambda_2)(1 - \lambda_3)\|}, \quad (7)$$

where  $\lambda_i$  are the eigenvalues of  $\phi_{,ij}^{(1)}$ . From this equation it is also clear the limit of perturbation theory: when  $\lambda_i \sim 1$ , the perturbative regime breaks down.

## 2.2 second-order Lagrangian Perturbation Theory

In order to derive the solution to the evolution of CDM particles, one must solve the equation of motion. If we approximate CDM particles as a pressure-less self-gravitating system in an expanding Universe, the equation of motion is

$$\frac{d^2}{d\tau^2} \mathbf{x} + \mathcal{H} \frac{d}{d\tau} \mathbf{x} = -\nabla \Phi(\mathbf{x}), \quad (8)$$

where we used the conformal time  $d\tau = dt/a$ , and  $\mathcal{H} = H/a$  and  $\Phi$  is the peculiar gravitational potential.

One can formally prove that at first order in Lagrangian perturbation theory, the solution consists of a scalar component only, and it is in fact the ZA (Eq. (5)). Moreover, the spatial component is separable from the time component, and we can write  $\psi^{(1)}(\mathbf{q}, \tau) = -\delta^{(1)}(\mathbf{q})D_1(\tau)$ . The time dependence is found from solving

$$\frac{d^2}{d\tau^2} D_1(\tau) + \mathcal{H} \frac{d}{d\tau} D_1(\tau) = \frac{3}{2} \Omega_m(\tau) \mathcal{H}^2 D_1(\tau). \quad (9)$$

The solution  $D_1$  is the linear growth function, and it is often replaced by fitting formulae rather than the exact solution. A widespread fitting formula for the growth function in a  $\Lambda$ CDM Universe is (Carroll et al. 1992)

$$D_1(a) \simeq \frac{5}{2} \frac{a\Omega_m(a)}{\Omega_m(a)^{4/7} - \Omega_\Lambda(a) + (1 + \Omega_m(a)/2)(1 + \Omega_\Lambda(a)/70)}. \quad (10)$$

Using a perturbative approach, it is possible to derive the solution at second order in perturbation theory, which reads

$$\psi^{(2)}(\mathbf{q}, \tau) = \frac{D_2(\tau)}{2D_1^2(\tau)} \sum_{i \neq j} \left( \phi_{,i,i}^{(1)} \phi_{,j,j}^{(1)} - \phi_{,i,j}^{(1)} \phi_{,j,i}^{(1)} \right), \quad (11)$$

where  $D_2$  is the second-order growth function, and  $\phi^{(1)}$  is the first-order displacement potential. Also in this case,  $D_2$  is separable and is solved perturbatively starting from  $D_1$ , but often one adopts the convenient fit (Bouchet et al. 1995)

$$D_2 \simeq -\frac{3}{7} D_1^2. \quad (12)$$

To summarize, the displacement in second-order Lagrangian perturbation theory (2LPT) is:

$$\Psi_{2\text{lpt}} = -\nabla \phi^{(1)}(\mathbf{q}, \tau) + \nabla \phi^{(2)}(\mathbf{q}, \tau), \quad (13)$$

where we defined the second-order displacement potential

$$\Psi^{(2)} = \nabla \phi^{(2)}. \quad (14)$$

One can push the perturbative treatment to higher orders, but the complexity increases as the scalar component receives a contribution from the curl component (Bouchet et al. 1995).

## 2.3 Spherical collapse and MUSCLE

A non-perturbative approach to model the scalar displacement field was proposed by Neyrinck (2013), who used a formula derivable from results in Bernardeau (1994) (see also Mohayaee et al. 2006). This formula approximates the evolution of isolated volume elements well. The MUSCLE approach obtains the displacement divergence

$$\psi_{\text{sc}} = \begin{cases} 3 \left[ \left(1 - \frac{\delta_\ell}{\gamma}\right)^{\gamma/3} - 1 \right], & \delta_\ell < \gamma \\ -3, & \delta_\ell \geq \gamma, \end{cases} \quad (15)$$

where  $\gamma$  is a parameter which in the limit of  $\Omega_{\text{cdm}} \sim 0$  is exactly 3/2. However, in using Eq. (15), the power spectrum of the generated density field is typically offset from the linear power spectrum on linear scales.

The reason for this linear-scale offset was made clear in the MUSCLE algorithm; SC misses the void-in-cloud process, which happens when a voxel density is under a collapse threshold on the grid scale, but over the threshold when smoothed on a larger scale. MUSCLE checks for collapse on increasingly larger scales of a linear density field smoothed through a window  $W(k)$

$$\delta_\ell(\mathbf{q}, R) = \int \frac{d^3k}{(2\pi)^3} e^{-i\mathbf{k}\cdot\mathbf{q}} \delta_\ell(\mathbf{k}) W(\mathbf{k}, R). \quad (16)$$

If  $\delta(\mathbf{q}, R) \geq \gamma$  at any scale  $R$ , then we set  $\psi(\mathbf{q}) = -3$ . The value of  $-3$  is indeed measured in halo particles from  $N$ -body simulations, and the multi-scale smoothing allows to check for overdense voxels that are expected to collapse at various scales.

## 2.4 Augmented Lagrangian Perturbation Theory

Before the appearance of MUSCLE, ALPT was proposed to remedy the large-scale power offset in SC more explicitly, by combining the 2LPT scalar divergence field with a low-pass filter and the SC formula of Eq. (15) with a high-pass filter (Kitaura & Hess 2013)

$$\psi_{\text{alpt}} = \psi_{2\text{lpt}} \otimes \mathcal{G}(\sigma_{\mathcal{R}}) + \psi_{\text{sc}} \otimes (1 - \mathcal{G}(\sigma_{\mathcal{R}})). \quad (17)$$

This is an interpolation between 2LPT on linear scales and SC on nonlinear scales. They are connected through a smoothing Gaussian kernel  $\mathcal{G}$ , where  $\sigma_{\mathcal{R}}$  is a free parameter of the approach, estimated to be around  $3 h^{-1} \text{Mpc}$  by a fit to  $N$ -body simulations.

In principle, the interpolation between large and small scales can be adopted also with MUSCLE, but it provides marginal improvement with respect to ALPT at the cost of a slightly greater computational cost due to the multi-scale smoothing required (Munari et al. 2017). For a detailed comparison between fast simulation schemes via the Lagrangian picture, we refer the reader to the reviews Monaco (2016); Munari et al. (2017).

## 3 METHOD

In this work, we compare approximate evolution of particles to the exact  $N$ -body results. Our simulation was run with GADGET (Springel 2005), starting at an initial redshift of  $z = 50$  and fiducial cosmology  $\Omega_b h^2 = 0.0225$ ,  $\Omega_{\text{cdm}} = 0.25$  and  $\sigma_8 = 0.8$ . This simulation has box-size  $256 h^{-1} \text{Mpc}$  and

a total of  $256^3$  particles. The initial conditions of the simulation have been generated through 2LPT, with amplitudes of the power spectrum fixed to the linear theory prediction (Angulo & Pontzen 2016). Throughout this work, we use the same initial conditions for the approximate schemes as well, so that we can quantify the agreement of an approximated scheme with reference simulation, at the level of a single realization.

Given any prescription for the scalar displacement field  $\psi$ , we can always connect it to the displacement potential by taking the divergence of Eq. (6)

$$\psi = -\nabla^2 \phi. \quad (18)$$

One can easily solve this equation for  $\phi$  in Fourier space, and finally compute the gradient to get the particle displacements through Eq. (6). The assumption of irrotationality has been numerically investigated by Chan (2014), who proved that the curl-free displacement field is an excellent approximation to the full  $\Psi$  up to scales of the order to  $k \sim 1 h \text{ Mpc}^{-1}$  even at  $z \sim 0$ .

To investigate the density field statistics, we estimate the density field on a Eulerian cubic grid of  $256^3$  cells by the means of a cloud-in-cell mass assignment scheme. We do not correct the mass assignment by exploiting the full procedure detailed by Jing (2005), but we only account for the effect of the window function by dividing our density estimates by the cloud-in-cell related kernel (Hockney & Eastwood 1988). The regime of validity of our results is well below the Nyquist frequency, so aliasing effects are negligible.

Among the statistics of the density field that we consider fundamental and that we examine in this work, the first is the PDF of the density field. The PDF is easily measured by counting the number of cells on the cubic grid with density  $[\delta, \delta + \Delta\delta]$  (Klypin et al. 2018)

$$P(\delta) = \frac{N_{\text{count}}(\delta)}{N_{\text{cell}}^3 \Delta\delta}, \quad (19)$$

normalized by the bin width. While the PDF of the density field has been often neglected over the years, it gained a renewed attention recently (e.g. (Uhlemann et al. 2016; Repp & Szapudi 2018; Tosone et al. 2020)).

Another fundamental statistic we analyze is the power spectrum  $P(k)$  of the density field, defined as

$$\langle \delta(\mathbf{k})\delta(\mathbf{k}') \rangle \equiv (2\pi)^3 \delta^{(D)}(\mathbf{k} + \mathbf{k}') P(k), \quad (20)$$

which quantifies the amplitude of the two-point correlation function.

Finally, we also examine the *similarity* between two density fields  $A$  and  $B$ , which is quantified by the cross-correlation

$$X(k) = \frac{\langle \delta_A(k)\delta_B^*(k) \rangle}{\sqrt{P_A(k)P_B(k)}}. \quad (21)$$

While it is always possible to generate two fields that have the same power spectrum, the cross correlation measures the similarity in the phases as well.

## 4 LIMITATIONS OF LAGRANGIAN APPROXIMATIONS

### 4.1 Truncation

In order to show the limitations of current semi-analytical Lagrangian techniques, we start by considering the truncation approach to model the displacement field. This approach was proposed by Coles et al. (1993), and it consists in cutting off the small scale power spectrum, just like in Eq. (16), with  $W(k)$  chosen as a Heaviside step function. The truncated density field is employed as usual in ZA, namely  $\psi_{TZA} = -\delta_\ell(R)$ , where  $\delta_\ell(R)$  is the linear density field truncated at a scale  $R$ . As a result, the real space cross-correlation coefficient between the approximated density field and the  $N$ -body field was found to improve with respect non-truncated schemes.

In the original implementation, a sharp cutoff for the window function  $W(k)$  was adopted. Melott (1994) reported a further improvement by adopting a Gaussian smoothing window. Ideally, the scale of cutoff should be the one that marks the onset of nonlinearities, when the variance of the density field is  $\sigma^2 \sim 1$ . While the cross correlation improves, the power spectra between truncated and non-truncated schemes remain similar, thus suggesting that the improvement is due to the better modelling of the *phases* of the field. Extending the truncation procedure to higher order corrections improves over the TZA (Buchert et al. 1994; Melott et al. 1995).

Truncated schemes perform well at the level of Fourier space cross correlation statistics as well, as we show in Fig. 1 for truncated 2LPT (T2LPT). For T2LPT we adopted an interpolation scale of  $2.5 h^{-1} \text{ Mpc}$  while for ALPT we used the a smoothing scale of  $3.0 h^{-1} \text{ Mpc}$ . They were chosen to maximize their cross correlations with the reference simulation, and were easily fine tuned by a simple inspection of a handful of different values. It is impressive that T2LPT yields something comparable to ALPT in the cross-correlation, even though T2LPT truncates all the information on small scales, which give overdense regions that are the first to collapse. However, as shown below in Fig. 8, T2LPT fails badly at modeling the PDF. This result suggests that the only benefit, at the level of cross-correlation, of the simple SC prescription in Eq. (15) is in its description of voids. But as we show below, the problem with the simple SC prescription is that it detects collapsed voxels too naively, looking for collapses only at the grid scale.

To test this hypothesis that the simple SC prescription is of little aid in modeling overdense regions, we reintroduce Eq. (15) by following the same baseline of ALPT: we augment T2LPT with the SC formula, so it is an augmented truncated Lagrangian perturbation theory (AT2LPT)

$$\psi_{\text{at2lpt}} = \psi_{\text{t2lpt}}(\sigma_R) + \psi_{\text{sc}} \otimes (1 - \mathcal{G}(\sigma_R)). \quad (22)$$

The large-scale component corresponds to T2LPT Gaussian smoothed at the scale  $\sigma_R$ , while the small scale component corresponds to the usual SC formula. Notice how, unlike in ALPT,  $\psi_{\text{t2lpt}}$  is not convolved with a window function because the convolution has been already applied to the linear density field.

One expects that including SC should improve the power spectrum or the cross correlation statistics. What we show in Fig. 1 is that this is not the case, and that AT2LPT

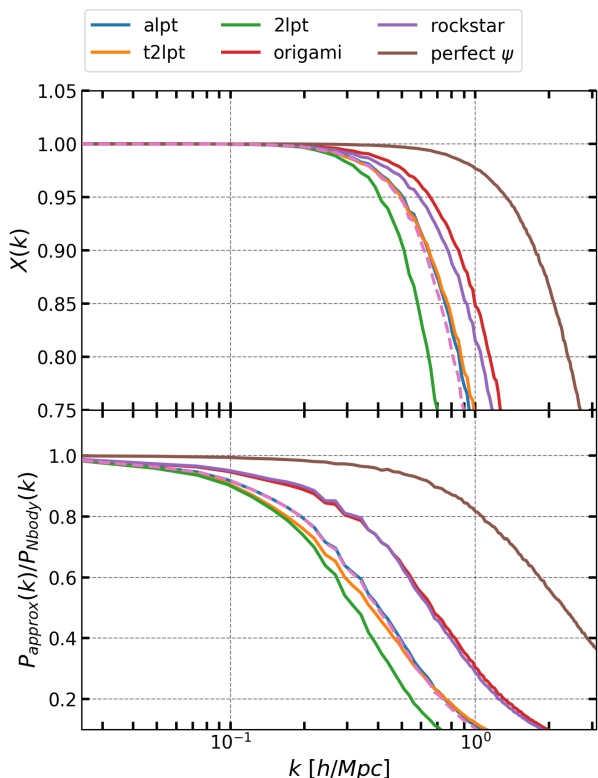


**Figure 1.** Cross correlation (top) and power spectrum (bottom) of the density field produced by the approximations of the displacement field considered in the text. Surprisingly, T2LPT approach performs as well as ALPT in these statistics, despite its poor modeling of the overdense regions. One can attempt to reintroduce the SC information with AT2LPT (the only dashed line), but it performs almost identically to ALPT and T2LPT. ORIGAMI and ROCKSTAR labels refer to approaches where the displacement field is modelled by Eqs. (23) and (24), namely the small scale component has been set to  $\psi = -3$  in correspondence of halo regions detected by these halo finders on the reference simulation (thus they are not predictive). This suggests that an improvement of Lagrangian approximations schemes should come from a better detection of overdense regions. Perfect  $\psi$  refers to the realization whose density field was generated by the curl-free displacement as measured from the  $N$ -body.

is in fact comparable to T2LPT, thus confirming that the only benefit of Eq. (15) is that it is an extremely good description of the evolution of voids, but we find that it does not perform as well in overdense regions. SC does not collapse structures in the same way as the  $N$ -body does, as shown in Fig. 2. We can see that the introduction of SC formula expands haloes and filaments with respect to T2LPT.

## 5 HALOES IN THE LAGRANGIAN PICTURE

Based on the results of truncated schemes, we realize that a shortcoming of Lagrangian approaches is a poor modelling of overdense regions.

First, we investigate whether tidal-field-related quantities could provide additional information to model the displacement field. One motivation for investigating the tidal

field is the success of the SC approach for void particles; this suggests that the ‘separate universe’ approximation to uncollapsed cells is highly accurate, even for anisotropic cells. Dai et al. (2015) found that corrections to a patch’s evolution are largely contained in the tidal field. Another motivation is that one can think of the eigenvalues as marking the onset of shell crossing, so they could be able to trace more closely halo formation and overdensities. While we find several correlations, none of them seem able to improve the modelling of  $\psi$  with respect to the standard linear density field. We show these results in Appendix A.

In the following discussion we focus on haloes. The advantage is that we already know how to model halo voxels in terms of the Lagrangian displacement, namely we just set  $\psi = -3$  (Neyrinck 2013). Our guess is that a more accurate detection of halo patches from the initial conditions yields an improvement in the statistics of the resulting density field. We can formally prove this by exploiting the *exact* information about halo regions, extracted from the reference simulation through halo finders.

### 5.1 Origami-informed realization

As anticipated, we use ORIGAMI (Falck et al. 2012) to detect halo particles in our reference simulation. We exploit this *a posteriori* information from the  $N$ -body result to realize a simulation whose displacement field has the same functional form as Eq. (22):

$$\psi_{\text{origami}} = \psi_{\text{t2lpt}}(\sigma_R) + \psi_{\text{ss}} \otimes (1 - \mathcal{G}(\sigma_{\mathcal{R}})), \quad (23)$$

but this time the small scale component  $\psi_{\text{ss}}$  is

$$\psi_{\text{ss}} = \begin{cases} -3, & \text{ORIGAMI halo regions,} \\ \psi_{\text{sc}} & \text{everywhere else,} \end{cases} \quad (24)$$

namely it is set to  $\psi = -3$  for halo voxels as found by ORIGAMI. All the non-halo regions are modeled with the SC formula, while T2LPT contributes to both halo and non halo regions on large scales. Without dwelling on the details, ORIGAMI is a Lagrangian halo finder which tracks the trajectories of the particles in the simulation to detect shell crossing events. Whenever trajectories overlap along a principal axis, one can consider that particles collapsed along that direction. The number and the direction of the collapses is indicative of the morphology of a particle.

In Fig. 1 we show the cross correlation and power spectrum statistics for this approach. We can see the noticeable improvement over ALPT, T2LPT and AT2LPT. This proves our point that the detection of halo regions alone could be the determining factor in modelling the displacement field. This improvement can also be seen in terms of particle displacements in Fig. 2: the displacement based on halo particles found through ORIGAMI is the closest to the actual  $N$ -body result.

### 5.2 Rockstar-informed realization

The way ORIGAMI detects haloes does not necessarily provide the same results as for the more standard Eulerian-based definition. We repeat the same procedure with halo particles detected by ROCKSTAR (Behroozi et al. 2013). We

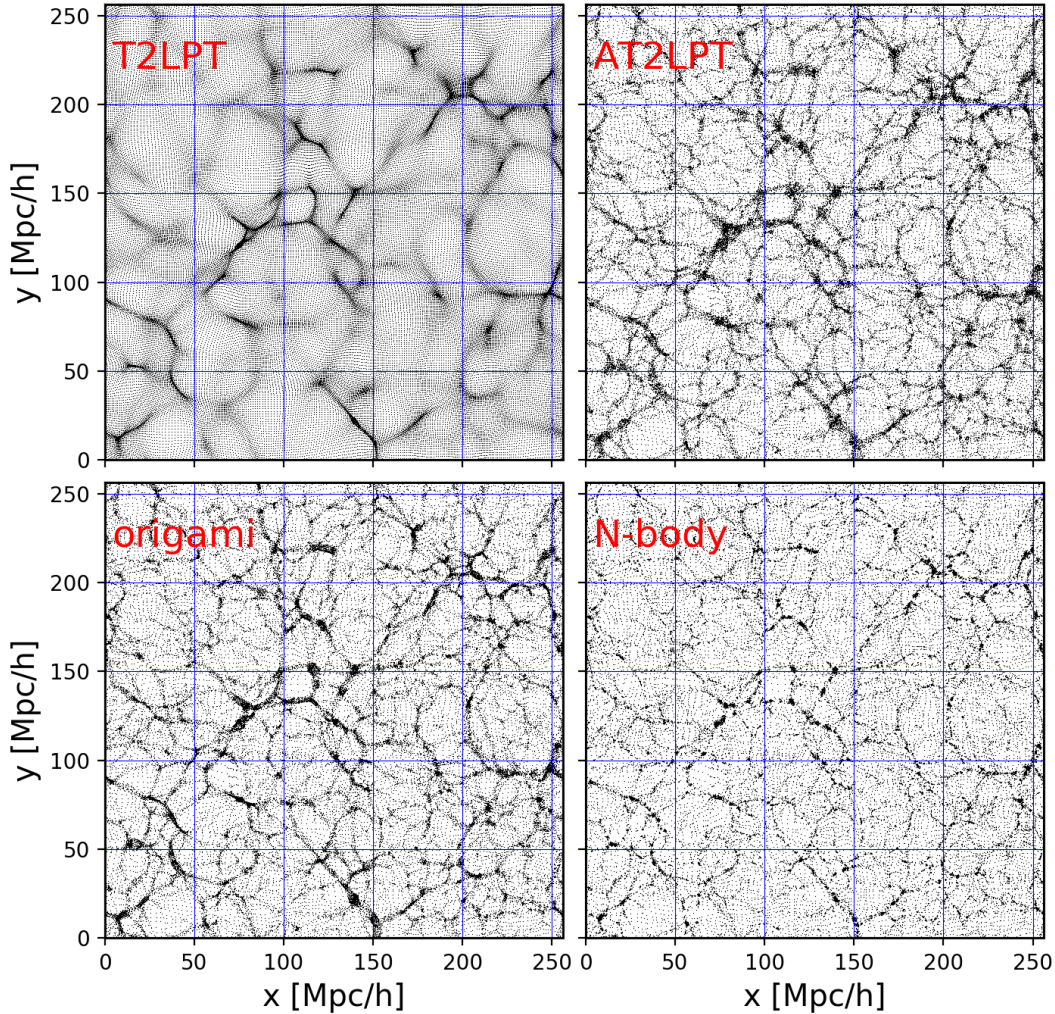


**Figure 2.** Eulerian positions of the particles in a  $1 h^{-1}\text{Mpc}$  thick slice of the simulations. One can notice how T2LPT traces well the cosmic web, but it is not able to reproduce collapses or voids. The augmentation of T2LPT with SC (Augmented Truncated LPT) recovers more correctly the voids, but it loses the benefit of truncation for filaments and haloes. The approach based on detecting halo particles through ORIGAMI is the one that looks more similar to the  $N$ -body.

find a comparable result to ORIGAMI (Fig. 1), which is surprising if we think about the difference in their baseline procedure to detect haloes. The similarity in the halo particles detected is also shown by Fig. 3.

For halo particles detected by ORIGAMI and ROCKSTAR, in Eq. (24) we substituted the actual value of  $\psi$  extracted from the reference  $N$ -body, finding virtually no change in  $X(k)$  and  $P(k)$  over the case of setting them to  $\psi = -3$ . This result further stress that the detection of halo particles is the main problem, and modelling them as  $\psi = -3$  suffices.

## 6 MULTISCALE SPHERICAL COLLAPSE LAGRANGIAN EVOLUTION USING PRESS-SCHECHTER

In this section we outline the algorithm we propose to predict more accurately which particles collapse into haloes from the initial conditions.

### 6.1 Extended Press and Schechter Formalism

In the following we refer to haloes in a Lagrangian sense; more correctly we refer to proto-haloes that can be detected through ORIGAMI and they do not necessarily correspond to haloes in the more common Eulerian sense and as they are found in standard halo finders. More on this is discussed at the end of section 7.

In Fig. 4 we show a slice of the scalar displacement field in various approximations. Haloes are dark patches with  $\psi \sim -3$ . It is clear that ALPT and MUSCLE cannot account for haloes at a level comparable to the  $N$ -body, but they seem to detect well the innermost regions of the halo patches as measured by ORIGAMI. This suggests that one could try to *expand these regions* to increase the resemblance with the  $N$ -body case.

One way to achieve this is to implement an algorithm whose basis is the same as in the EPS formalism: if the linear density field smoothed at a scale  $R$  is above a threshold at a point  $\mathbf{x}$  in the initial conditions, i.e.  $\delta_\ell(\mathbf{x}, R) > \delta_c$ , all the

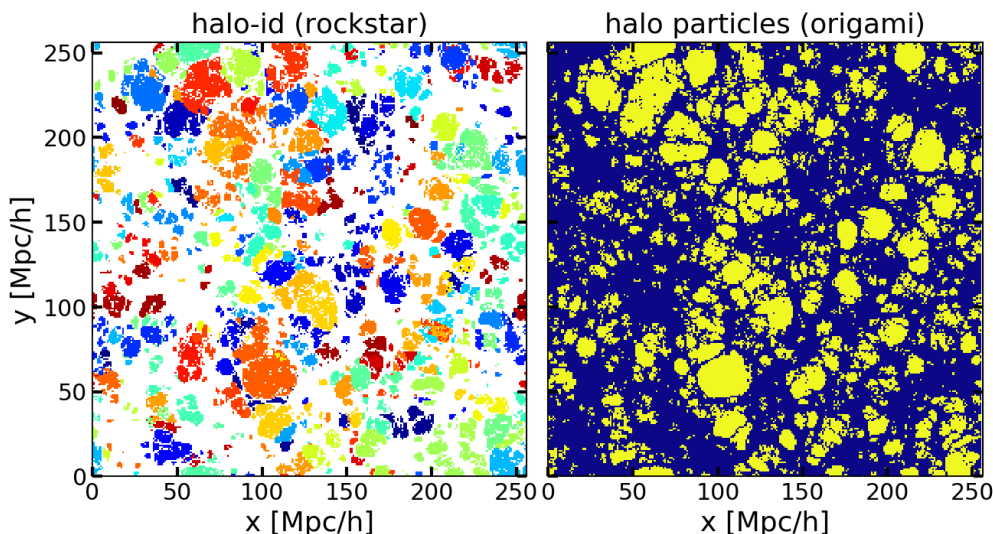


**Figure 3.**  $1 h^{-1}\text{Mpc}$  thick slice of the initial conditions. On the left, we show halo particles color coded based on their halo-id, as found by ROCKSTAR. On the right we show halo particles as found by ORIGAMI. Their agreement is rather high, considering the difference in their baseline process.

particles that are within a distance  $R$  from  $\mathbf{x}$  form a halo of mass  $M = 4\pi\rho_m R^3/3$  (Press & Schechter 1974), where  $\rho_m$  is the average matter density of the Universe. Also, the fact that these patches are contiguous and that setting  $\psi = -3$  is a good approximation (Section 5), suggests that  $R$  should be defined in such a way that it corresponds to the largest scale at which the halo collapses.

The EPS formalism is not exploited by Lagrangian schemes. The only similar process can be found in MUSCLE, since halo regions are detected through the multi-scale smoothing of the linear density field, but MUSCLE is ultimately voxel-based as the condition  $\psi = -3$  is set independently for each voxel.

The adaptation of the EPS formalism to the Lagrangian picture is to set  $\psi = -3$  for all the voxels within the patch identified by the smoothing filter. Intuitively, it is reasonable to consider that a voxel does not undergo a standalone collapse, especially if the collapse criterion is satisfied at scales larger than the inter-particle separation. Also, it is already known that the standard SC criterion may succeed to detect the peaks but fail to capture the patch (Ludlow & Porciani 2011).

It is not self-evident how to practically implement a Lagrangian EPS, as one could choose different types of window functions for the smoothing, and argue about the fraction of voxels enclosed within the smoothing window. As a matter of fact, only in the case of a top-hat window function

$$W(k) = 3 \frac{\sin(kR) - kR \cos(kR)}{(kR)^3}, \quad (25)$$

it is immediate to consider it as a proto-halo of size  $R$ ; it becomes less obvious for general window functions like a Gaussian one

$$W(k) = e^{-k^2 R^2/2}. \quad (26)$$

For example, it was already noted by Bond & Myers (1996) that the mass enclosed in a proto-halo of size  $R$  identified through a Gaussian filter would correspond to a proto-

halo size of about  $R/2$  with a top-hat filter, if we impose that they enclose about the same mass.

To illustrate the different results from the choice of different filters, in Fig. 5 we compare the power spectra obtained with MUSCLE by adopting both a top-hat and Gaussian window function for detecting the halo particles. The original implementation of MUSCLE makes use of a Gaussian, and slightly underestimates the power spectrum, while a top-hat based MUSCLE implementation generally has a slightly larger amplitude than the reference power spectrum. This difference comes from the number of halo particles detected: in the top-hat case the condition for collapse is satisfied to a maximum scale that can be as large as twice the maximum scale of collapse of the Gaussian window, thus detecting more halo particles, which are responsible for the offset of the power spectrum even on linear scales.

## 6.2 MUSCLE-UPS

Among all the possible choices for the smoothing window to detect halo patches, we opt for an EPS scheme with a Gaussian window: all the particles that are within a radius  $R$  from a voxel where the condition of SC is satisfied are set to  $\psi = -3$ . With this choice there is a close correspondence with the halo patches as found through ORIGAMI, as shown in Fig. 4.

This approach has the counter effect of increasing substantially the number of halo particles, and it does introduce the problem that the amplitude of the power spectrum overshoots the amplitude of the target spectrum, even though we are using a Gaussian window (Fig. 5). Luckily we already know how to circumvent this limitation, i.e. by interpolating the large scales, where we already established that T2LPT is a good choice, with the small scales, where now we have a better description for halo particles. The first part of our proposed algorithm, dubbed MULTIscale Spherical Collapse Lagrangian Evolution Using Press-Schechter (MUSCLE-UPS),

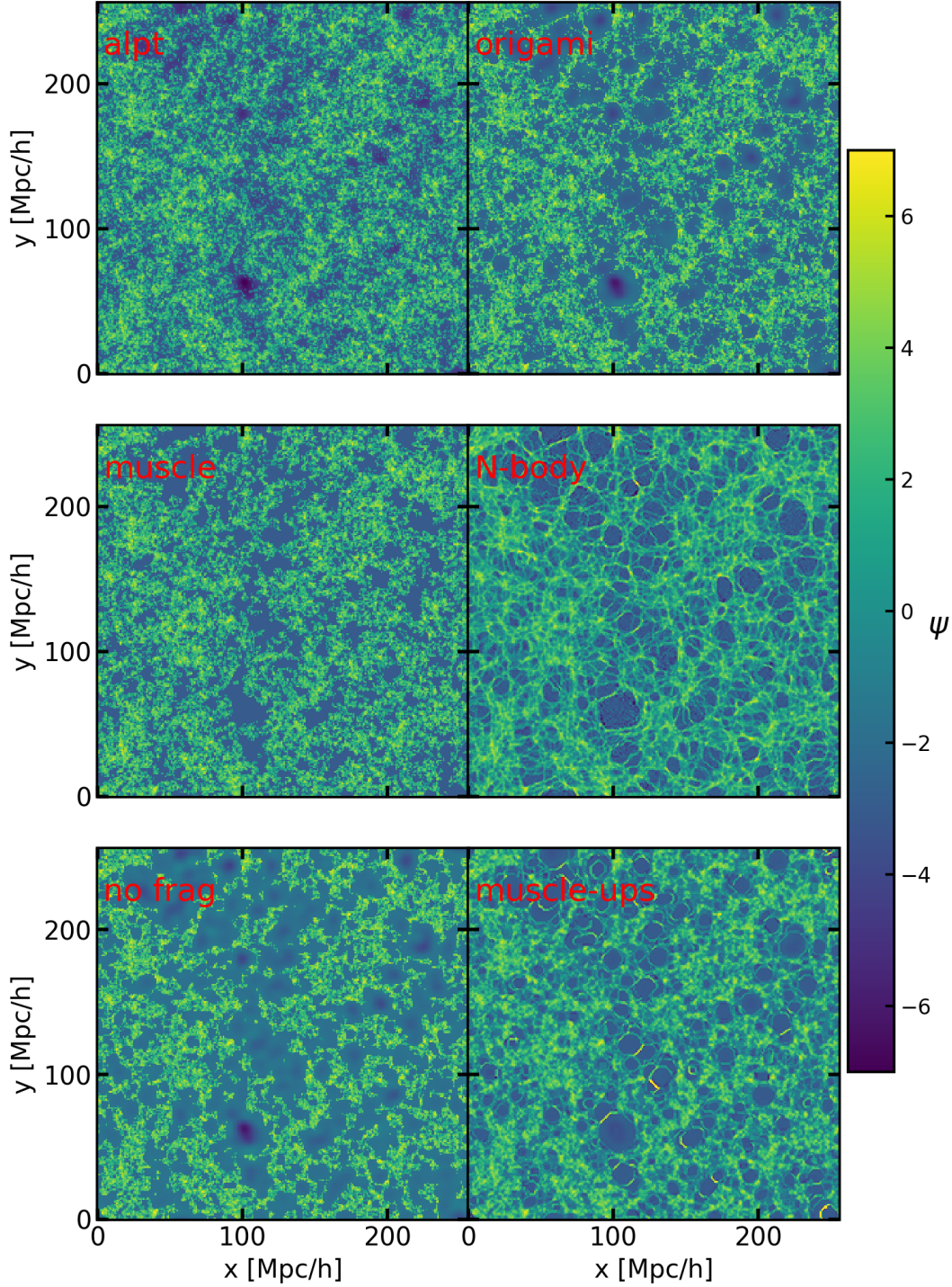


**Figure 4.** One-particle-thick Lagrangian slice of the displacement field of the various approximation schemes. Particles have been colour-coded based on the value of  $\psi$ . ALPT and MUSCLE can trace well the innermost halo voxels when compared to ORIGAMI and N-body. Our method of expanding them further according to Eq. (27) is shown in the bottom left panel. It increases the similarity to the N-body, with the caveat that there is no fragmentation between the halo patches. In Section 7 we explain how the fragmentation can be reintroduced with the addition of a halo model, as shown in the bottom-right panel.

reads

$$\psi_{\text{muscleups}} = \psi_{\text{2lpt}}(\sigma_R) + (\psi_{\text{eps}} + \psi_{\text{sc}}) \otimes (1 - \mathcal{G}(\sigma_R)), \quad (27)$$

$$\psi_{\text{eps}}(\mathbf{q}) = -3, \text{ if } \mathcal{S}_R[\delta_\ell](\mathbf{y}) > \gamma \text{ for any } \mathbf{y} \in \mathcal{B}_R(\mathbf{q}) \text{ and } R \geq 0;$$

$$\psi_{\text{sc}}(\mathbf{q}) = 3 \left[ \left( 1 - \frac{\delta_\ell(\mathbf{q})}{\gamma} \right)^{\gamma/3} - 1 \right], \text{ otherwise.} \quad (29)$$

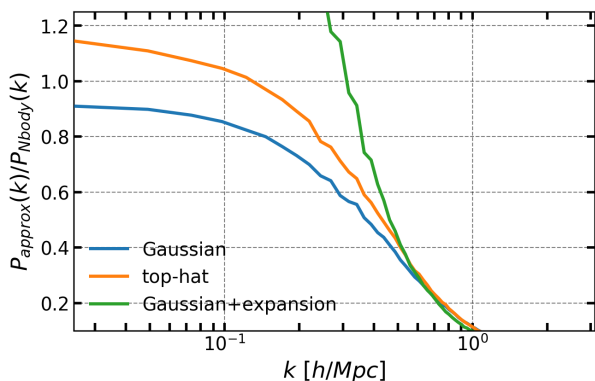


**Figure 5.** Difference in the power spectrum through MUSCLE with Gaussian and top-hat filters. The increased power of the top-hat case is attributed to a increased number of halo particles. The linear power dramatically increases when we expand haloes. This offset can be correct by implementing an interpolation in order to match the large-scale power to perturbation theory predictions, as prescribed in Eq. (27).

Here we used the notation

$$\mathcal{B}_R(\mathbf{q}) = \{\mathbf{y} \text{ s.t. } d(\mathbf{q}, \mathbf{y}) \leq R\} \quad (30)$$

to refer to the ‘ball’ of points which are at most at a distance  $R$  away from  $\mathbf{q}$ . Eq. (27) clarifies that our approach is the combination of T2LPT truncated at the scale  $\sigma_R$  for the large-scale component, *augmented* with a modification of MUSCLE for the small scale component. This modification is made up of Eq. (28), which states that whenever the smoothed density field  $\mathcal{S}_R[\delta_i]$  collapses at any scale  $R$ , including the trivial case of the inter-particle distance, we should set  $\psi = -3$  for all the neighbouring voxels within a distance  $R$  from the voxel under examination. If the condition of collapse is never met, Eq. (29) is used. Even if a voxel does not meet the condition for collapse, it could still have  $\psi = -3$  if it is near a collapsing voxel.

As in MUSCLE, we perform the smoothing process by starting from the inter-particle distance, and progressively going to larger distances; this process stops as soon as a scale where no voxel collapse is reached. Also, we increase the number of smoothing filters to cover all the possible discrete lengths in units of inter-particle distance. Just like in MUSCLE and in SC, the process of setting all the voxels to the same value introduces a nonzero average  $\langle \psi \rangle = C$  that must be subtracted to preserve the zero mean density condition.

From Fig. 4 we can see that the bare result of Eq. (27), labelled *no frag*, has a limitation: halo patches are not fragmented into separate haloes as in  $N$ -body. In the following section, we complete our MUSCLE-UPS algorithm by addressing this issue.

## 7 IMPLEMENTING A HALO MASS FUNCTION AND THE HALO MODEL

The natural follow-up to the multi-scale smoothing of the initial density is to build a halo catalogue, and to fragment the  $\psi = -3$  patches into haloes. In this way MUSCLE-UPS can output a displacement for CDM particles and for the

haloes as well, which is more useful for the purpose of mock galaxy catalogues.

There are already EPS based algorithms available, such as PEAK-PATCH (Bond & Myers 1996) and PINOCCHIO (Monaco et al. 2002). In this section we show how we can build a halo catalogue as well, with a simpler approach than what they proposed, but reaching higher precision for the HMF. Finally we also add the halo model in order to mimic the collapse of the particles of the of proto-haloes.

### 7.1 Building a halo catalogue

The main idea of the EPS formalism is that haloes form from overdense patches of size  $R$  that are found to collapse in the linear density field, according to the SC criterion. The cloud-in-cloud problem of the original argument by Press and Schechter (Press & Schechter 1974) was addressed in the EPS approach by considering the largest patches that collapse by the redshift under examination (Bond et al. 1991; Bond & Myers 1996). This is based on the argument of a hierarchical structure formation, where a large object formed by processes of mergings of smaller haloes or by accretion, thus subsuming the smaller overdensities.

For each particle, we save the largest smoothing scale at which it collapses, if it collapses at all. We dub the array containing this information the *sift field*; in analogy to sifting grains, it stores the hole size at which a particle falls through the sifter. This can be stored in terms of units of the inter-particle distance, thus as an integer.

The sift field alone does not suffice to build a catalogue, as we have a discrete number of smoothing filters and many candidate haloes which share the same smoothing scale. Thus we also store the *collapse condition field*  $cc = 1 - \delta_\ell(\mathbf{x}, R)/\gamma$ , evaluated at the value  $R$  of the sift field, for each collapsing particle. It suffices to create these two arrays at the beginning of the bottom up filtering process, so that for each particle we can save or update the largest smoothing scale at which the collapse condition is verified, stored in the sift field, alongside the corresponding density stored in the cc field.

We use the sift field and the cc field to implement a simple hierarchical structure formation scenario. We first group the halo candidates, saved in the sift field, by their smoothing scale. For each smoothing scale we reorder the candidates in increasing order of the cc field values, namely in order of decreasing smoothed linear density. We then create a new integer array that stores the halo-id of each particle, so that particles belonging to the same haloes share the same tag.

The list of particles in the sift field identifies the center of proto-haloes. Starting from the largest and densest halo candidate in our list, we cycle through all the particles within a distance  $R$  from its center, where  $R$  is its smoothing scale. The same unique halo-id is assigned to each particle only if (1) the particle has  $\psi = -3$ , namely it is considered a halo particle, and (2) the particle has not been assigned a unique halo-id yet. Clearly this does not happen for the first halo candidate, but it may happen for the following proto-haloes in the list. If a particle has a halo-id already assigned, it means that the particle already belongs to another larger and denser halo that overlaps with the one under examination, and so the particle is not assigned a new id.

When a candidate halo particle in the sift field has al-

ready a halo-id assigned to it, it means that its patch lies within a larger or denser patch. In this case there are a couple of ways to proceed: (1) either we discard it, or (2) we merge it to the parent halo.

In Fig. 6 we present the HMF resulting from the first scenario, where no merging occurs because a hard exclusion criterion is applied. We see that it drastically fails when compared to both the theoretical prediction of Tinker et al. (2008) and the HMF measured from our reference simulation with ROCKSTAR. In particular, we see that a Gaussian-based EPS results in both an excess of small haloes and in a complete lack of large haloes, which suggests that mergings are necessary when a Gaussian filter is adopted. On the other hand, in the case of a top-hat smoothing function as in the standard EPS scenario, more haloes are found at higher masses, and the resulting HMF seems a better approximation to the expected HMF, even without mergings. However, its predictions are not quantitatively reliable, and we would like to develop an algorithm that yields a HMF closer to the expected result; the Gaussian filter allows more freedom to do this.

Attempting to predict the formation and the merging of haloes from the initial conditions at the level of each individual object is a daunting task. PEAK-PATCH and PINOCCHIO are the only software that attempted this, with some success. Here we propose a different scheme that exploits the excess of small haloes candidates detected through Gaussian smoothing; the great deal of freedom in merging these halo candidates allows us to build a halo catalogue that can reproduce the HMF measured from  $N$ -body simulations. The idea is to insert a halo candidate in the catalogue or to perform a merging between two haloes if and only if this improves the resulting HMF by making it closer to the target. This means that we need to update the resulting HMF on the fly for every merging or whenever a new candidate halo is inserted in the catalogue. But this process is cheap considering that we already have a list of all the possible haloes.

The result of this process is plotted in Fig. 6, where we can see that it minimizes the residuals with respect to the target HMF, being extremely precise over a large mass range. It is worth stating explicitly that this optimization procedure of the HMF is not stochastic, but it is fully determined from the initial conditions once the internal parameters of the algorithm have been specified. These internal parameters include the number of smoothing scales in the initial conditions, that we fixed to cover all the possible discrete lengths in units of inter-particle distance, and the sampling of the target HMF. The sampling has only one free parameter, the width of the mass bin  $\Delta \log(M/(M_\odot/h))$ . In fact, the mass of the smallest halo is implicitly fixed by the mass resolution of the simulation, while the largest expected halo has a mass that can be easily computed from the target HMF, knowing the box-size of the simulation. We tried several resolutions for the width of the mass bins, finding little variation for a high number of bins. The results we present here were obtained with a width of  $\Delta \log(M/(M_\odot/h)) = 0.025$ .

There is a caveat in our result: by matching exactly a template HMF, we cannot reproduce the intrinsic fluctuations that exist in the HMF measured in the reference  $N$ -body with the same initial conditions. In other words, the variance of the measured HMF from many realizations run

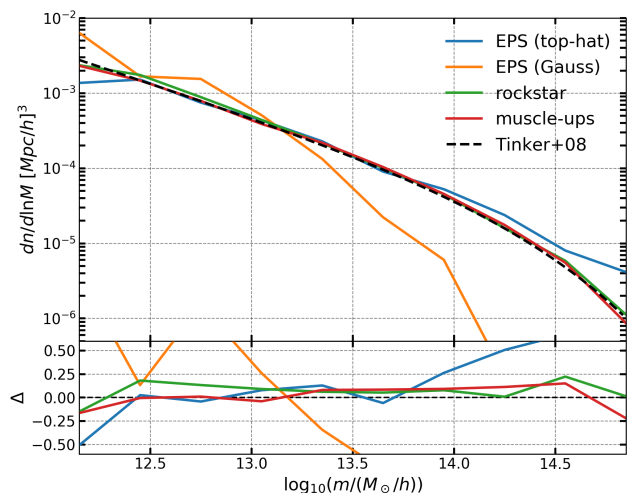


**Figure 6.** In the top panel we show the HMFs obtained in various scenarios. *EPS (Gauss)* refers to an EPS approach with a Gaussian window function, when no mergings occur. Analogously for the *EPS (top-hat)* result. In *MUSCLE-UPS* we implement the scheme discussed in the text based on merging Gaussian protohaloes to match a target HMF. The *ROCKSTAR* label corresponds to the HMF measured directly from the reference simulation. In the bottom panel we show the relative residuals with respect to the fit provided by Tinker et al. (2008), which we chose as the target HMF and whose implementation is found in *COLOSSUS* (Diemer 2018).

with our scheme is expected to be smaller than the corresponding variance from  $N$ -body realizations. We do not have a solution for this, but arguably this problem also affects, in a different way, the standard EPS formalism: the fluctuations of the HMF estimated from the initial conditions do not coincide with those measured in the Eulerian HMF at low redshift.

We have not yet specified the threshold  $\gamma$  of the collapse condition that we adopted in this work. The choice of  $\gamma$  is predicted from linear perturbation theory to be 1.69 for a standard cosmology. In Stein et al. (2019) it was found that this value underestimates the number of candidate haloes, and a value equal to 1.5 was used. The same value of 1.5 is also found independently as a fit to optimize the SC predictions through a machine learning algorithm (Lucie-Smith et al. 2018). Coincidentally, the same value is also the one that was originally used by Bernardeau (1994) in his original proposal of Eq. (15), motivated by the solution to the evolution of a void embedded in a homogeneous universe; for these reasons we decided to keep it as it is.

As a first final thought, we would like to underline that the fragmentation process is, of course, not exact. Even if we could identify with perfect accuracy the halo particles in the initial conditions, it is still not obvious how to group them into halo patches. Fig. 3 shows the similarity of the halo particles detected between *ORIGAMI* and *ROCKSTAR*, but there is not a one-to-one correspondence between an *ORIGAMI* isolated patch and the halo-id as found from *ROCKSTAR*. We cannot build a Eulerian HMF from the *ORIGAMI* morphology alone, and some choices based on the density field must be made (Falck et al. 2012). The HMFs from *ORIGAMI* and *ROCKSTAR* are indeed found to be different; by detecting only

particle crossings and not testing for gravitational boundedness, ORIGAMI tends to identify larger patches than ROCKSTAR (Knebe et al. 2011).

To conclude, we highlight the differences of MUSCLE-UPS with respect to PEAK-PATCH, that we take as a reference for a numerical implementation of EPS. PEAK-PATCH first detects overdense patches in the field through a top-hat window function; afterwards, haloes are built around the densest voxel in each patch by including spherical shells, until the overdensity  $\Delta$  of the halo is below a certain threshold. Finally, proto-haloes are collapsed by making some assumption about the dynamics.

MUSCLE-UPS works only at the level of the patches, detected through a Gaussian window. We do not explicitly build the halo around the densest voxel in each patch. While the regions where  $\psi = -3$  are round, due to the voxel expansion process of Eq. (27), the way patches are fragmented into halos does not require any spherical symmetry, and patches can be aspherical. Due to the fact that Gaussian proto-patches are much smaller than their top-hat counterparts, we can merge them to match a target HMF, instead of trying to get the HMF directly from the top-hat proto-patches. To conclude, unlike PEAK-PATCH and PINOCCHIO, we do not need to assume the dynamics of collapse, as we find more natural to evolve the particles first according to the displacement of Eq. (27), and then displace them in Eulerian space to match the expected halo density profile. This is explained in the following.

## 7.2 Implementing the Halo Model

The working hypothesis of the halo model is that all the matter in the Universe is found in virialized haloes, although this is a simplification (Angulo & White 2010). The halo model power spectrum of CDM can be written as the combination of two contributions: the large-scale correlations between haloes, commonly referred as the two-halo term, and the correlation between particles inside the same halo, the one-halo term, (Peacock & Smith 2000; Seljak 2000)

$$P(k) = P_{2h}(k) + P_{1h}(k). \quad (31)$$

Schemes like PEAK-PATCH and PINOCCHIO use this assumption, as they solve the equations for the ellipsoidal collapse of a homogeneous sphere for all proto-haloes, overdense with respect to the background, which are then displaced according to perturbation theory. Implicitly this corresponds, in terms of the displacement field, to

$$\psi = \psi_{2h} + \psi_{1h}. \quad (32)$$

We prefer to follow an alternative approach to this problem: since we already created a halo catalogue from the initial conditions, one could redistribute particles that have been tagged with the same halo-id into a Navarro Frenk and White (NFW) density profile (Navarro et al. 1996), directly in Eulerian space. This avoids disentangling the two-halo displacement from the one-halo displacement, which is anyway unknown and potentially entangled to the two-halo term in a nonlinear way. We can first displace particle according to a Lagrangian scheme of our choice, and then we redistribute them into NFW haloes, as we explain in Appendix C.

This scheme recalls the PTHALOE procedure in redistributing particles directly in Eulerian space (Scoccimarro & Sheth 2002; Manera et al. 2013). The difference is that PTHALOE is a fundamentally Eulerian approach: after the 2LPT displacement of particles is run, a halo finder is employed to detect the densest regions (with a very large linking length, necessary because 2LPT haloes are far overdispersed. These are fragmented to match the desired HMF, and their particles are sampled from NFW profiles. In contrast, in order to match the correct HMF, our fragmentation is implemented in the initial conditions, during the compilation of the halo catalogue.

## 8 DENSITY FIELD STATISTICS FROM MUSCLE-UPS

We start to examine the results by first looking at the particle displacements in Fig. 7. In the simpler case where no fragmentation of haloes is implemented, we can see the improvement over ALPT anyway. This is reflected in a more defined cosmic web, where haloes and filaments are clearly more compact. This is much more similar to the results obtained through the *a posteriori* simulation based on ORIGAMI in Fig. 2, where the exact information on halo particles is exploited. The only caveat that we can notice is that some regions, especially large dense ones, have particles which are scattered around and collapsed neither to haloes nor filaments. We checked that these particles are in fact halo particles ( $\psi = -3$ ), and this effect might be an artefact of the patch expansion process, that includes a larger fraction of halo particles than the simulation predicts, and it is due to halo patches not being well fragmented (see Fig. 4).

This is indeed confirmed by the final MUSCLE-UPS implementation, where this effect disappears and these extra particles are effectively collapsed onto haloes, while the overall cosmic web is not disrupted. It is actually possible to see that there is an excellent correspondence between the knots in the  $N$ -body and the ones in the halo model approximation.

The effects of the halo fragmentation are also apparent in Fig. 4, at the level of the displacement field. For the first time, we are able to show that the filamentary structure of the  $\psi$  field, not to be confused with density field filaments, is related to the collapse of haloes. In  $N$ -body, these thin discs between haloes stretch out to form filaments, whereas in MUSCLE-UPS, they are often only a particle thick, indicating a displacement between haloes that may not be filled in with filament particles between them. While perfect correspondence with the  $N$ -body displacement field cannot be expected, it is still impressive to see that a toy halo model added *by hand* can qualitatively reproduce this feature. We notice how these  $\psi$ -filaments are rounder than what is observed in the  $N$ -body. While we did not impose any sphericity in grouping particles into haloes, it seems that the halo patch expansion is still the dominant effect in determining the shape of proto-halo patches. We also note that our NFW algorithm retains the order of particle distances in raw MUSCLE-UPS away from the halo core, which produces a smooth  $\psi$  field inside each halo. In  $N$ -body, the difference between the Lagrangian and Eulerian ordering in haloes is

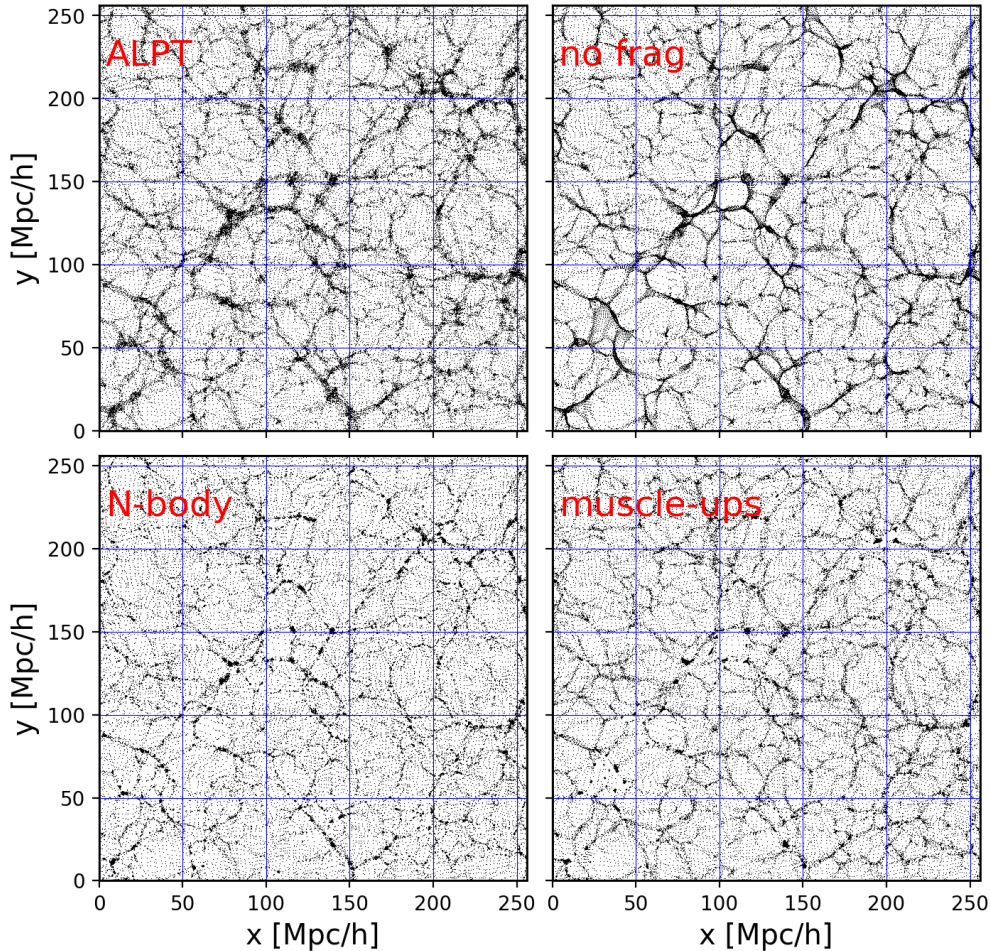


**Figure 7.** Eulerian positions of the particles in a  $1 h^{-1}\text{Mpc}$  thick slice of the simulations. We plot the MUSCLE-UPS displacement without the fragmentation into haloes in the upper right panel, where one can notice the improvement over ALPT in collapsing filaments and haloes, which we attribute to the increased size of halo patches, that make the result more similar to what we obtained through ORIGAMI. However some of the particles are not collapsed at all. This issue can be corrected by incorporating a halo model (bottom right panel), where these particles are redistributed into NFW haloes as found in the initial conditions.

generally rather random, which is made apparent by the noise inside the halo-patches in  $\psi$  there.

We now examine the statistics of the density field, starting with the PDF plotted in Fig. 8. A pure perturbation theory based scheme like 2LPT fails drastically to account for the tails. The PDF is even worse for T2LPT, where the voids are completely unaccounted for. The benefit of SC (Eq. (15)) formula becomes apparent in ALPT, where the low density tails improves thanks to a better description of voids. MUSCLE-UPS further improves the modelling of the voids, thanks to the multi-scale modelling, but the most apparent gain in using the halo model is clear at the high density tail.

In Fig. 9 we show the results for the cross correlation and the power spectrum statistics at various redshifts. Looking at the cross correlation statistic, we can see that there is a marginal increase at all the redshifts. At  $z = 0$  and  $k = 1 h \text{ Mpc}^{-1}$ , we find 0.79 for our implementation against 0.71 for ALPT. Although this gain in the cross correlation looks marginal at first glance, it is in fact a remarkable improve-

ment; it is much harder to improve this statistic than the power spectrum.

Concerning the power spectrum, there is a recovery of power in the quasi linear regime. This recovery is much similar to what we achieved through ORIGAMI and ROCKSTAR *a posteriori* realizations in Fig. 1. To quote some numbers, at  $k = 0.1 (0.3) h \text{ Mpc}^{-1}$  and redshift  $z = 0$ , we find that the accuracy of the matter power spectrum measured from a realization generated with MUSCLE-UPS, is about 5% (18%). This is marginally better than ALPT that has 8% (37%). As we go to higher redshifts, the improvement becomes more apparent; at the same wavenumbers we quote 1% (1.1%) against 3% (14%) of ALPT.

In both ALPT and MUSCLE-UPS there is an interpolation scale,  $\sigma_R$ , which is a free parameter. We fix it to  $3.0 h^{-1}\text{Mpc}$  at  $z = 0.0, 0.43$  and  $2.5$  and  $1.8 h^{-1}\text{Mpc}$  at  $z = 1.0, 1.83$  respectively for MUSCLE-UPS. For ALPT we fix  $\sigma_R$  to  $3.0 h^{-1}\text{Mpc}$  at  $z = 0.0, 0.43$  and  $2.0 h^{-1}\text{Mpc}$  at  $z = 1.0, 1.83$ . The value of  $\sigma_R$  decreases as we go to higher redshift, since the SC regime starts at the very smallest scales and becomes less relevant. We set this value by try-

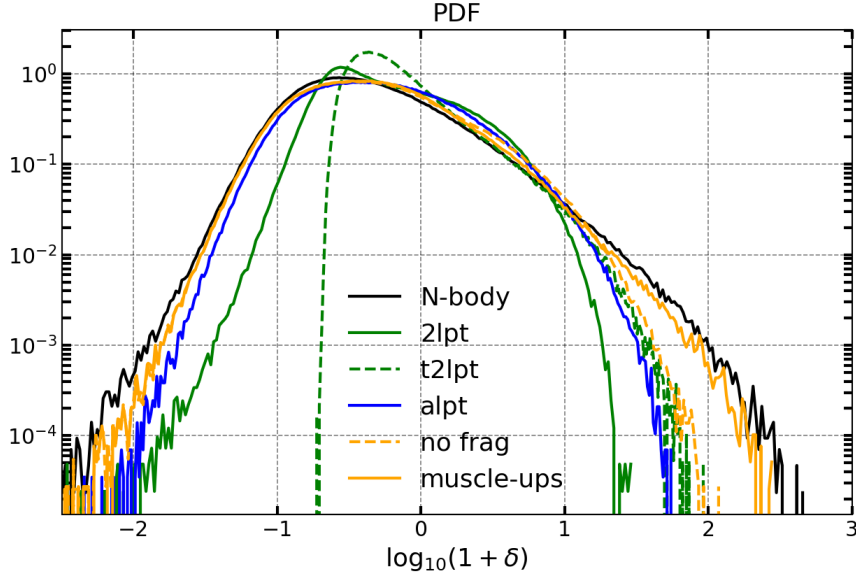


**Figure 8.** Eulerian PDF of the density field generated through various approximation schemes. The density field has been measured from the  $256^3$  particles on a mesh grid of  $128^3$  cells, with a cloud-in-cell mass assignment scheme. The density field has been corrected in Fourier space for the effect of the mass assignment with the related cloud-in-cell kernel (Hockney & Eastwood 1988).

ing a handful of them, and choosing the one that gives the highest the cross correlation.

We find a strong dependence of the one-halo term of the power spectrum on the halo-model ingredients. For example, the results we discussed so far have been obtained by using twice the concentration of Eq. (B5). This results in a shallow increase in the power spectrum for the one-halo term. By using the exact relation of Bullock et al. (2001) instead, we find that haloes are much smaller than what is seen in the  $N$ -body Fig. 7, and the resulting power spectrum would show a sharp increase in power soon after the transition from large scales to the nonlinear regime, alongside with a decrease of the cross correlation (which becomes comparable to the no-fragmentation implementation of MUSCLE-UPS). It could be possible that the concentration value can be tuned differently at each redshift, thus improving even further the agreement.

Another way to affect both  $P(k)$  and  $X(k)$  is to change the sampling of the target HMF (Section 7). We find that a finer mass resolution helps to increase  $X(k)$  with a slight decrease in  $P(k)$ . Last, also the interpolation scale of ALPT is relevant for  $X(k)$  and  $P(k)$  statistics, with a higher scale that results in a higher power spectrum and a lower cross correlation. In this study we did not optimize the combination of all these parameters, as the results we obtained seem pretty stable under their changes, or affected mostly at the level of the smaller scales.

## 9 SUMMARY & CONCLUSIONS

In this work we presented MUSCLE-UPS, a semi-analytical Lagrangian simulation scheme to approximate the displacement of CDM particles. MUSCLE-UPS is based on the observation that the SC criterion implemented with a Gaussian window detects the innermost regions of proto-halo patches.

Since the collapse of particles into haloes is not a standalone process, one should expand these halo voxels to include neighbouring voxels, exploiting a similar concept behind the numerical implementation of the EPS formalism; this prescription increases the resemblance to the  $N$ -body result (Fig. 4).

Expanding the halo voxels has the counter effect of increasing the number of halo particles, which in turn increases the linear power spectrum (Fig. 5). We adopt the same ansatz of ALPT by interpolating the displacement field on small scales with perturbation theory on large scales. Formally, the Lagrangian displacement of MUSCLE-UPS, without the halo model, is summarized by Eq. (27).

There is a degree of arbitrariness on how to expand the halo voxels; we find an approach that works well by considering all the particles within a distance  $R$  from a collapsing voxel, where  $R$  is the scale of the Gaussian filter applied to the linear density field to detect the collapse. We find that the adoption of a Gaussian filter is crucial, as a top-hat window seems to overestimate the collapsing regions, even without expanding them. In addition, the use of a Gaussian window allows us to find many smaller proto-halos when compared to top-hat based EPS, which then can be merged together to match a HMF based on the freedom in the choice of merging events among the many candidate haloes (Fig. 6). Finally, we used this halo catalogue to implement a toy halo model.

The generation of the displacement field Eq. (27) is rather fast, and comparable to MUSCLE, as most of the computational time spent is spent to perform the multi-scale smoothing of the initial conditions. However, in its complete form, MUSCLE-UPS has higher complexity than MUSCLE, as most of the computational time is spent in matching the target HMF by sifting through the halo candidates. However, this process can be greatly optimized through parallelization

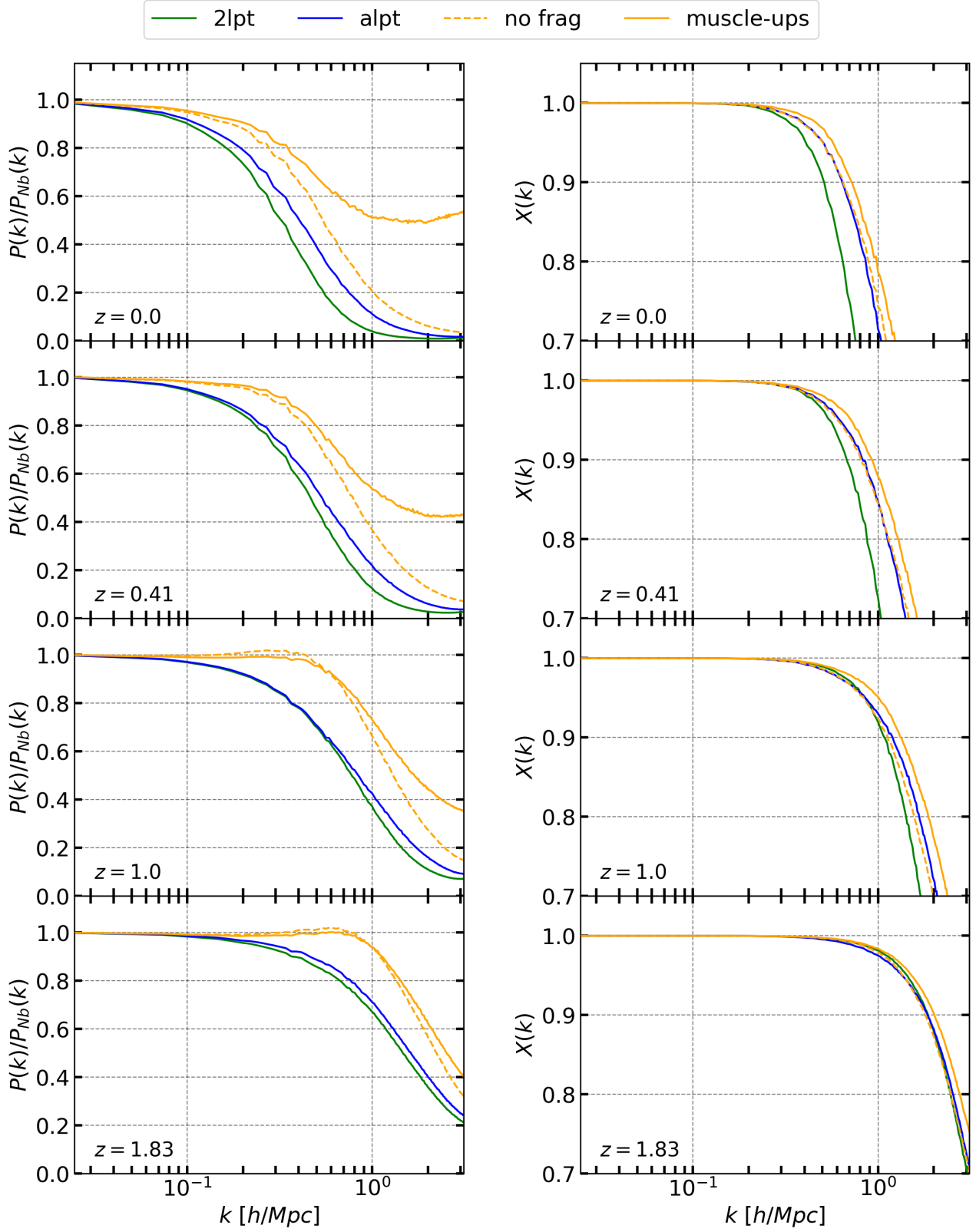


**Figure 9.** Power spectra and cross-correlations of the density fields generated through ALPT, MUSCLE-UPS and 2LPT, compared to the density field of an  $N$ -body simulation run with the same initial conditions. The label *no frag* refers to the realization where particles have not been fragmented into haloes, but only displaced according to Eq. (27).

by dividing the grid into subgrids, a task that we leave for a different work.

The improvement of MUSCLE-UPS over previous schemes is apparent from the particle displacement (Fig. 7); one can see that voids are accurately described, the cosmic web is preserved as in  $N$ -body, and haloes are collapsed. This result is quantified by the PDF (Fig. 8), the power spectrum and the cross correlation (Fig. 8) of the density field.

While an exact modelling of the small scale dynamics still eludes us, our approach improves the resemblance to the exact result at least on a statistical level. In fact, for the first time we are able to reproduce the filamentary structure of the displacement field (Fig. 4), finding that it emerges as a consequence of collapse into haloes.

## ACKNOWLEDGEMENTS

FT thanks the Dipartimento di Fisica ‘‘Aldo Pontremoli’’ of the University of Milano, and the Dept. of Theoretical Physics (now simply the Dept. of Physics) at the University of the Basque Country in Bilbao for hospitality during the development of this work. LG, BRG and FT acknowledge financial support by grant MIUR PRIN 2017 ‘‘From Dark-light to Dark Matter.’’ MCN is grateful for funding from Basque Government grant IT956-16. FT is grateful to Enzo Branchini and Carmelita Carbone for useful discussions.

## APPENDIX A: TIDAL FIELD

The connection of tidal fields to the cosmic web has been known for a long time (Bond & Myers 1996). Tidal effects can be expressed in terms of the eigenvalues of the shear tensor, that we already defined in Section 2.1 from Eq. (4). This tensor can be readily computed in Fourier space

$$\partial_{ij}\phi^{(1)} = \mathcal{F}^{-1} \left[ k_i k_j \phi^{(1)}(\mathbf{k}) \right], \quad (\text{A1})$$

where  $\mathcal{F}^{-1}$  stands for the inverse Fourier transform. In the ZA limit  $\psi^{(1)} \sim -\delta$ , so that the displacement potential is

$$\phi^{(1)}(k) = -\frac{\delta^{(1)}(k)}{k^2}, \quad (\text{A2})$$

and the stress tensor is defined as

$$\partial_{ij}\phi = \mathcal{F}^{-1} \left[ -\frac{k_i k_j}{k^2} \delta^{(1)}(\mathbf{k}) \right]. \quad (\text{A3})$$

By diagonalizing the shear tensor matrix at every point  $\mathbf{q}$ , one can use the eigenvalue fields  $\lambda_1 \leq \lambda_2 \leq \lambda_3$  instead of the full matrix expression. This is convenient in the linear theory limit, where one can regard the moment where  $|\lambda| \sim 1$  as the onset of shell crossing along that particular eigen-direction. Ultimately, this can be used as an approximation to classify the morphology of the cosmic web from the initial conditions (Hahn et al. 2007), or to express the anisotropy of the asphericity of gravitational collapse (Sheth & Tormen 2002).

We thus analyze the correlations between the eigenvalues and the displacement field in order to see if there is some unexploited information contained in the fields of the eigenvalues. Unfortunately, Fig. A1 shows that there is a high amount of correlation between  $\delta_\ell$  and  $\lambda_i$ , which can be expected since  $\delta_\ell = \lambda_1 + \lambda_2 + \lambda_3$ . In fact, we find that it is also

possible to define the displacement solely in terms of the first eigenvalue, i.e. a mapping  $\psi(\lambda_1)$ , but it performs similarly to the approximation schemes discussed in Section 2 based on  $\psi(\delta_\ell)$ .

We do not rule out the possibility that complicated non-linear combinations of the eigenvalues could exist, which may be related to  $\psi$  in a non-trivial way. We investigate this scenario by considering the cosmic web invariants (Kitaura et al. 2020)

$$\begin{aligned} I_1 &= \lambda_1 + \lambda_2 + \lambda_3, \\ I_2 &= \lambda_1 \lambda_2 + \lambda_1 \lambda_3 + \lambda_2 \lambda_3, \\ I_3 &= \lambda_1 \lambda_2 \lambda_3, \\ I_4 &= \lambda_1^2 + \lambda_2^2 + \lambda_3^2, \\ I_5 &= \lambda_1^3 + \lambda_2^3 + \lambda_3^3. \end{aligned} \quad (\text{A4})$$

Cosmic web invariants are fundamental fields which can be used to define all the tidal field related quantities of interest, such as ellipticity, prolateness and fractional tidal anisotropy (e.g. Paranjape et al. (2018)). An extensive analysis of cosmic web invariants and their relation to the Eulerian halo field was performed by Kitaura et al. (2020), where they justify them as a way of fully characterizing the cosmic web. We instead consider them in relation to the Lagrangian displacement field, i.e. defined through the linear eigenvalues. From Fig. A2, one can see how the only significant correlation, apart from the trivial one with  $I_1$ , is the one with  $I_5$ . Unfortunately  $I_5$  is also highly correlated with  $\delta_\ell$ . The limit of the amount of information carried by  $\delta_\ell$  in relation to  $\psi$  was already shown in Tosone et al. (2020).

## APPENDIX B: HALO MODEL INGREDIENTS

For a review about the halo model and its ingredients we refer the reader to Cooray & Sheth (2002); here we summarize the main quantities we need in the following. The NFW density profile is (Navarro et al. 1996)

$$\rho_{\text{nfw}}(r) = \frac{\bar{\rho}_m(z) \Delta_v(z) f(c)}{c \frac{r}{r_v} \left(1 + c \frac{r}{r_v}\right)^2}, \quad (\text{B1})$$

$c$  is the concentration parameter, that can be regarded as a rescaling that modulates the density of the profile.  $r_v$  is the virial radius, namely the radius which contains the virial mass  $M$  of the halo, corresponding to an overdensity  $\Delta_v(z)$  (e.g.  $\sim 178$  in Einstein de Sitter). These quantities must be related by mass conservation relation

$$M = \frac{4\pi}{3} r_v^3(z) \bar{\rho}_m \Delta_v(z). \quad (\text{B2})$$

For the nonlinear spherical overdensity at virialization  $\Delta_v$ , we use the fitting formula by Bryan & Norman (1998)

$$\Omega_m(z) \Delta_v(z) = 18\pi^2 + 82(\Omega_m(z) - 1) - 39(\Omega_m(z) - 1)^2. \quad (\text{B3})$$

The normalization function  $f(c)$  is derived under the assumption that all the mass of the halo is within the virial radius, thus by integrating Eq. (B1) and truncating the integration at the virial radius, one can solve for the normalization

$$f(c) = \frac{c^3}{3 \left( \ln(1+c) - \frac{c}{1+c} \right)}. \quad (\text{B4})$$

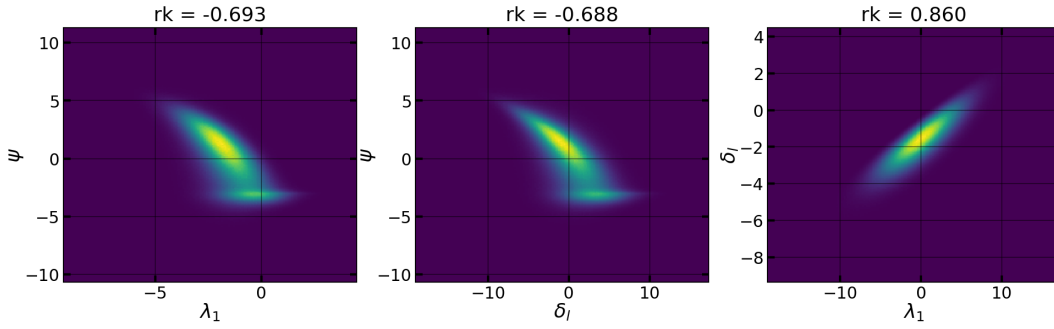


**Figure A1.** Plots of the correlation between the displacement field and the linear theory eigenvalues. The value on top is the Spearman's rank correlation coefficient.

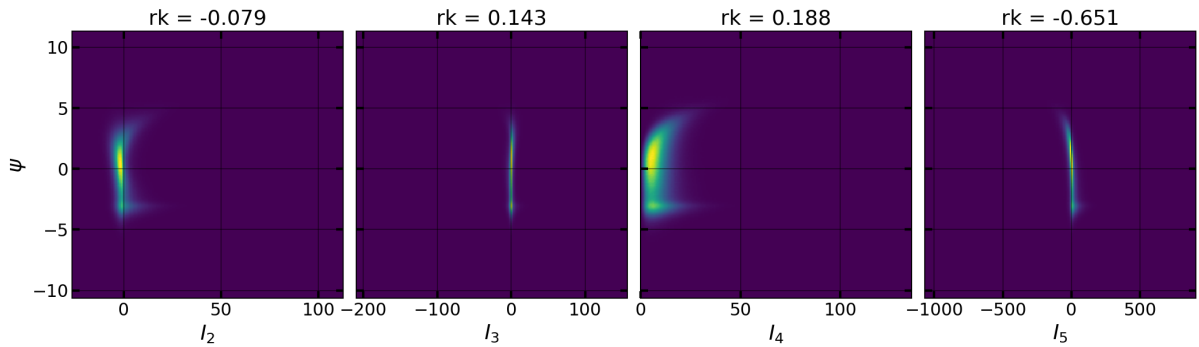


**Figure A2.** Correlation of the cosmic web invariants with the displacement field  $\psi$ . The value on top is the Spearman's rank correlation coefficient. Apart from  $I_1 = \delta_\ell$ , only  $I_5$  seems to be correlated with the displacement. Unfortunately the Spearman's rank correlation between  $I_5$  and  $\delta_\ell$  is about 0.95, which shows how it does not provide new information with respect to the linear density.

The concentration parameter encompasses important information about the cosmological model and structure formation (Mead 2017). In this work we use the median relation found by Bullock et al. (2001)

$$c(M) = \frac{9}{1+z} \left( \frac{M}{M_*(z)} \right)^{-0.13}, \quad (\text{B5})$$

where  $M_*$  is the critical mass such that  $\sigma(M_*, z) = \delta_c$ . This formula has been validated for a vanilla  $\Lambda$ CDM cosmology, for haloes in the mass range  $\sim 10^{11} - 10^{14} M_\odot/h$ , thus it adapts well to the present study and to the mass resolution we considered. Despite the halo model in this form is rather raw, and it is already known that there are refined fits for the concentration parameters or halo profiles (Wang et al. 2019), we stick to it because of its simplicity. Also, we do not expect that a halo model, regardless of the precision of the fitting formulae we adopt, can be precise enough to recover exactly the  $N$ -body result, as the halo model remains an extreme useful simplification of the actual matter distribution.

### APPENDIX C: REDISTRIBUTING HALO PARTICLES

As we said in Section 6, particles are first displaced according to a Lagrangian scheme of our choice, which in our case is set by Eq. (27). Since we already have the halo catalogue, we just need to redistribute particles with the same halo-id according to a NFW profile directly in Eulerian space.

For each halo, we first find its barycenter, then we use the expected nonlinear overdensity Eq. (B3) to compute the virial radius from Eq. (B2). The halo density profile is then completely specified by Eqs. (B4) and (B5). To redistribute the particles of each halo around its barycenter according to a NFW profile, we first rank-order the particles based on their distances from the barycenter, which corresponds to the cumulative distribution function (CDF) of the halo profile. Afterwards, the inverse CDF of the NFW density profile is used in order to displace particles according to desired distribution.

While this can be done in a fully numerical approach, Robotham & Howlett (2018) found out that the inverse CDF of a NFW profile has an analytical form. To see this we define the dimensionless variable  $q = r/r_v$  that indicates the distance from the halo center. The mass enclosed at a distance  $q$  from the center is

$$M(q) \propto \ln(1+qc) - \frac{qc}{1+qc}. \quad (\text{C1})$$

It is convenient to define the cumulative distribution function of the enclosed mass, which is simply  $p = M(q)/M(1)$ , where the total mass is  $M = M(1)$ , and to recast the previous equation by adding 1 on both sides

$$pM(1) + 1 = \ln(1+qc) + \frac{1}{1+qc}. \quad (\text{C2})$$

We exponentiate this equation, and exploit the fact that it is possible to invert it by the means of the Lambert function  $W$ . In other words the transcendental relation  $y = e^{1/x}$

can be inverted as  $x = -1/W(-y^{-1})$ . An implementation of the Lambert function is found in the GNU Scientific Library<sup>1</sup>. By applying it to Eq. (C2), we get (Robotham & Howlett 2018)

$$q = -\frac{1}{c} \left( 1 + \frac{1}{W(-e^{-pM(1-1)})} \right), \quad (\text{C3})$$

namely a procedure that allows to preserve the rank ordering of the halo particles, by mapping each rank  $p$  to a distance  $q$  from the center.

The previous procedure could reduce the asphericity of the haloes, as they are redistributed as an NFW profile. We then try to preserve the triaxiality by adopting the same scheme used in Mead & Peacock (2014). The first thing is to compute the inertia tensor of each halo, before its particles are redistributed

$$I_{ij} = m_p \sum_{k=1}^N \left( |\Delta \mathbf{x}^{(k)}|^2 \delta_{ij} - \Delta x_i^{(k)} \Delta x_j^{(k)} \right), \quad (\text{C4})$$

where  $\Delta x_i^{(k)}$  is the  $i$ -th component of the  $k$ -th particle, and  $\Delta x_i^{(k)} = x_i^{(k)} - \bar{x}_i$  is the distance from the halo barycenter along the  $i$ -th direction. For each halo, we diagonalize the tensor and save its eigenvalues and eigenvectors. After particles have been distributed to match the NFW profile, we restore the triaxiality by rescaling each  $i$ -th particle in the halo along its eigendirections by a factor proportional to the eigenvalues (Mead & Peacock 2014)

$$\begin{aligned} \Delta x_i &= 3a \Delta x_i / (a + b + c), \\ \Delta y_i &= 3b \Delta y_i / (a + b + c), \\ \Delta z_i &= 3c \Delta z_i / (a + b + c), \end{aligned} \quad (\text{C5})$$

with  $a, b, c$  being the square root of the eigenvalues of  $I_{ij}$ .

## REFERENCES

- Angulo R. E., Pontzen A., 2016, *MNRAS*, **462**, L1  
 Angulo R. E., White S. D. M., 2010, *MNRAS*, **405**, 143  
 Avila S., Murray S. G., Knebe A., Power C., Robotham A. S. G., Garcia-Bellido J., 2015, *MNRAS*, **450**, 1856  
 Behroozi P. S., Wechsler R. H., Wu H.-Y., 2013, *ApJ*, **762**, 109  
 Bernardeau F., 1994, *ApJ*, **427**, 51  
 Bond J. R., Myers S. T., 1996, *ApJS*, **103**, 1  
 Bond J. R., Cole S., Efstathiou G., Kaiser N., 1991, *ApJ*, **379**, 440  
 Bond J. R., Kofman L., Pogosyan D., 1996, *Nature*, **380**, 603  
 Bos E. G. P., Kitaura F.-S., van de Weygaert R., 2019, *MNRAS*, **488**, 2573  
 Bouchet F. R., Colombi S., Hivon E., Juszkiewicz R., 1995, *A&A*, **296**, 575  
 Bryan G. L., Norman M. L., 1998, *ApJ*, **495**, 80  
 Buchert T., 1992, *MNRAS*, **254**, 729  
 Buchert T., Melott A. L., Weiss A. G., 1994, *A&A*, **288**, 349  
 Bullock J. S., Kolatt T. S., Sigad Y., Somerville R. S., Kravtsov A. V., Klypin A. A., Primack J. R., Dekel A., 2001, *MNRAS*, **321**, 559  
 Carroll S. M., Press W. H., Turner E. L., 1992, *ARA&A*, **30**, 499  
 Chan K. C., 2014, *Phys. Rev. D*, **89**, 083515  
 Chuang C.-H., Kitaura F.-S., Prada F., Zhao C., Yepes G., 2015, *MNRAS*, **446**, 2621  
 Coles P., Melott A. L., Shandarin S. F., 1993, *MNRAS*, **260**, 765  
 Cooray A., Sheth R. K., 2002, *Phys. Rept.*, **372**, 1  
 Dai L., Pajer E., Schmidt F., 2015, *J. Cosmology Astropart. Phys.*, **2015**, 059  
 Diemer B., 2018, *ApJS*, **239**, 35  
 Falck B. L., Neyrinck M. C., Szalay A. S., 2012, *ApJ*, **754**, 126  
 Hahn O., Porciani C., Carollo C. M., Dekel A., 2007, *Monthly Notices of the Royal Astronomical Society*, **375**, 489  
 Hockney R. W., Eastwood J. W., 1988, *Computer Simulation Using Particles*. Taylor & Francis, Inc., USA  
 Jasche J., Wandelt B. D., 2013, *MNRAS*, **432**, 894  
 Jing Y. P., 2005, *ApJ*, **620**, 559  
 Kitaura F. S., 2013, *MNRAS*, **429**, L84  
 Kitaura F. S., Hess S., 2013, *MNRAS*, **435**, L78  
 Kitaura F. S., Yepes G., Prada F., 2014, *MNRAS*, **439**, L21  
 Kitaura F.-S., et al., 2016, *MNRAS*, **456**, 4156  
 Kitaura F.-S., Balaguera-Antolínez A., Sinigaglia F., Pellejero-Ibáñez M., 2020, arXiv e-prints, p. arXiv:2005.11598  
 Klypin A., Prada F., Betancort-Rijo J., Albareti F. D., 2018, *Mon. Not. Roy. Astron. Soc.*, **481**, 4588  
 Knebe A., et al., 2011, *MNRAS*, **415**, 2293  
 Leclercq F., Jasche J., Wandelt B., 2015, *JCAP*, **1506**, 015  
 Lucie-Smith L., Peiris H. V., Pontzen A., Lochner M., 2018, *MNRAS*, **479**, 3405  
 Ludlow A. D., Porciani C., 2011, *MNRAS*, **413**, 1961  
 Manera M., et al., 2013, *MNRAS*, **428**, 1036  
 Mead A., 2017, *Mon. Not. Roy. Astron. Soc.*, **464**, 1282  
 Mead A. J., Peacock J. A., 2014, *MNRAS*, **440**, 1233  
 Melott A. L., 1994, *ApJ*, **426**, L19  
 Melott A. L., Buchert T., Weiss A. G., 1995, *A&A*, **294**, 345  
 Mohayaee R., Mathis H., Colombi S., Silk J., 2006, *MNRAS*, **365**, 939  
 Monaco P., 2016, *Galaxies*, **4**, 53  
 Monaco P., Theuns T., Taffoni G., 2002, *Mon. Not. Roy. Astron. Soc.*, **331**, 587  
 Monaco P., Sefusatti E., Borgani S., Crocce M., Fosalba P., Sheth R. K., Theuns T., 2013, *Mon. Not. Roy. Astron. Soc.*, **433**, 2389  
 Munari E., Monaco P., Koda J., Kitaura F.-S., Sefusatti E., Borgani S., 2017, *JCAP*, **1707**, 050  
 Navarro J. F., Frenk C. S., White S. D. M., 1996, *ApJ*, **462**, 563  
 Neyrinck M. C., 2013, *MNRAS*, **428**, 141  
 Neyrinck M. C., 2016, *MNRAS*, **455**, L11  
 Padmanabhan N., Xu X., Eisenstein D. J., Scalzo R., Cuesta A. J., Mehta K. T., Kazin E., 2012, *MNRAS*, **427**, 2132  
 Paranjape A., Hahn O., Sheth R. K., 2018, *Monthly Notices of the Royal Astronomical Society*, **476**, 3631  
 Peacock J. A., Smith R. E., 2000, *Mon. Not. Roy. Astron. Soc.*, **318**, 1144  
 Press W. H., Schechter P., 1974, *ApJ*, **187**, 425  
 Repp A., Szapudi I., 2018, *MNRAS*, **473**, 3598  
 Robotham A. S. G., Howlett C., 2018, *Research Notes of the American Astronomical Society*, **2**, 55  
 Scoccimarro R., Sheth R. K., 2002, *MNRAS*, **329**, 629  
 Seljak U., 2000, *Mon. Not. Roy. Astron. Soc.*, **318**, 203  
 Sheth R. K., Tormen G., 2002, *MNRAS*, **329**, 61  
 Springel V., 2005, *MNRAS*, **364**, 1105  
 Stein G., Alvarez M. A., Bond J. R., 2019, *MNRAS*, **483**, 2236  
 Tassev S., Zaldarriaga M., Eisenstein D. J., 2013, *Journal of Cosmology and Astro-Particle Physics*, **2013**, 036  
 Tinker J., Kravtsov A. V., Klypin A., Abazajian K., Warren M., Yepes G., Gottlöber S., Holz D. E., 2008, *ApJ*, **688**, 709  
 Tosone F., Neyrinck M. C., Granett B. R., Guzzo L., Vittorio N., 2020, *MNRAS*, **498**, 2663  
 Uhlemann C., Codis S., Pichon C., Bernardeau F., Reimberg P., 2016, *MNRAS*, **460**, 1529  
 Wang J., Bose S., Frenk C. S., Gao L., Jenkins A., Springel V., White S. D. M., 2019, arXiv e-prints, p. arXiv:1911.09720

<sup>1</sup> <https://www.gnu.org/software/gsl/doc/html/specfunc.html>

Zentner A. R., 2007, [International Journal of Modern Physics D](#),  
**16**, 763

This paper has been typeset from a  $\text{T}_{\text{E}}\text{X}/\text{L}^{\text{A}}\text{T}_{\text{E}}\text{X}$  file prepared by  
the author.